



# Utilization of a MnO<sub>2</sub>/polythiophene/rGO nanocomposite modified glassy carbon electrode as an electrochemical sensor for methyl parathion

T. Ramachandran<sup>1</sup> · V. Violet Dhayabaran<sup>1</sup>

Received: 13 February 2019 / Accepted: 27 May 2019 / Published online: 1 June 2019  
© Springer Science+Business Media, LLC, part of Springer Nature 2019

## Abstract

The present work describes the utility of an inexpensive modified electrode for the electrochemical detection of an organophosphorus pesticide, methyl parathion (MP). A glassy carbon electrode was modified with MnO<sub>2</sub>/PTH/rGO nanocomposite (where PTH = polythiophene and rGO = reduced graphene oxide), which was prepared by in situ chemical oxidative polymerization method. Its morphology, diffraction, impedance and electrochemical measurement were studied using FTIR, XRD, Raman spectra, SEM, HR-TEM with EDX, cyclic voltammetry, differential pulse voltammetry and amperometric techniques. The modified glassy carbon electrode of MnO<sub>2</sub>/PTH/rGO film delivers an excellent electrocatalytic ability due to the presence of MnO<sub>2</sub> and rGO. It also exhibited a high sensitivity of 0.0498  $\mu\text{A } \mu\text{M}^{-1} \text{cm}^{-2}$  and limit of detection (LOD) of 5.72 nM. A synergistic effect of the components rGO, PTH and MnO<sub>2</sub> accounts for high sensitivity, selectivity, acceptable reproducibility and good stability, which characterizes a promising tool for ultrasensitive detection of methyl parathion. Besides, practical possibility of the sensor was demonstrated in biological samples which delivered excellent recovery results.

## 1 Introduction

Nano-electroanalytical chemistry is one of the most researched area in nanotechnology and nanocomposite studies. Hitherto, electrochemical detection of pesticides in biomolecules was achieved using hybrid nanocomposite materials. Pesticides are routinely used in agriculture to increase the crop yields [1–3]. Among the commonly used pesticides, more than 38% are organophosphorus (OPs) compounds. Methyl parathion (MP) is a class of organophosphorus insecticides, classified to be ‘Category Ia’ (extremely toxic) by the World Health Organization (WHO) [4, 5]. Due to the extensive use of MP, the pesticide residues enter the human body through air, water, soil and food materials at trace concentrations [6, 7]. Unfortunately, MP exhibits high toxicity to both humans and animals owing to bioaccumulation. This

compound is known to irreversibly inhibit acetylcholinesterase (AChE) in the presence of OPs, an enzyme involved in the catalysis of neurotransmitters like acetylcholine (ACh) and choline esters. As a result, it leads to respiratory failure, impairment of thoracic skeletal muscle function and eventually, death due to accumulation of phosphorylated AChE in the synaptic cleft of affected neurons. [8, 9]. Therefore, the Environmental Protection Agency (EPA) faces a daunting task of detecting pesticide contamination and hence, analytical methods have been devised for the determination of pesticides [10–19]. Even though, these techniques have significant merits such as reasonably low limit of detection, accuracy, sensitivity, etc., there are some drawbacks such as high cost, longer time consumption, usage of toxic organic solvents and necessity of highly trained personnel [20, 21]. This prompted us to develop an effective method to meet essential requirements such as high sensitivity, selectivity, low limit of detection and easy handling.

Nowadays, next generation devices in the electroanalytical field have made detection and identification rather simple, because of the development and utilization of modified electrodes. In recent years, detection of pesticides using nanomaterial-based modified electrodes, such as Au/rGO, poly (malachite green) graphene-nafion composite, silver/graphene nanoribbons and polymer based multi-walled

**Electronic supplementary material** The online version of this article (<https://doi.org/10.1007/s10854-019-01590-9>) contains supplementary material, which is available to authorized users.

✉ V. Violet Dhayabaran  
violetstaff@yahoo.co.in

<sup>1</sup> Department of Chemistry, Bishop Heber College, Tiruchirappalli, Tamil Nadu 620 017, India

carbon nanotube modified electrodes [22–26] have been successfully employed for pesticide detection.

Over the past few decades, graphene-based nanocomposites are being used extensively as electrochemical sensors owing to their advantages such as large surface area, catalyst supports, high electrical conductivity, well defined pore size, thermal stability, and usefulness as electrochemical sensors [7, 27]. Recently, conducting polymers such as polyaniline based electrochemical sensor for the detection of pesticide are becoming popular due to their synergistic effects [28]. In addition, some researchers have reported utility of combined inorganic oxide nanoparticles with organic conducting polymeric hybrid materials as effective sensors due to the special synergistic properties of both individual components [29]. Manganese oxide ( $\text{MnO}_2$ ) has been considered as one of the most attractive transition-metal inorganic materials. It has been used in energy storage devices and biosensor techniques because of its high electrical properties, flexibility, low cost and environmental friendliness [30, 31] Polythiophene (PTH) is an organic conducting polymer used in many fields, such as sensors, supercapacitors, catalysts and in chemically stable electrode materials [32, 33].

Herein, we report the preparation of  $\text{MnO}_2$ /PTH/rGO nanocomposite material by using in situ chemical polymerization. The electrochemical performance of the  $\text{MnO}_2$ /PTH/rGO modified electrode and its specificity for MP was investigated. Under optimized conditions, the nanocomposite modified electrode exhibited better performance in the monitoring of MP with faster response, lower limit of detection and better sensitivity when compared to the unmodified GC electrode. To the best of our knowledge, this type of polymer based composite material has not been previously used for MP detection. In this work, the sensor has been successfully employed for analysis of MP in real samples such as human blood, serum and urine using the  $\text{MnO}_2$ /PTH/rGO modified GC electrode.

## 2 Experimental

### 2.1 Materials

Methyl parathion (MP) (99.9%), nafion and thiophene (99.9%) was purchased from Sigma-Aldrich (Pune, India). The stock solution of MP was prepared using acetone. Phosphate buffer solution (PBS) was prepared with a standard stock solution of  $\text{K}_2\text{HPO}_4$  (99% purity) and  $\text{KH}_2\text{PO}_4$  (99% purity). Unless otherwise it is explicitly stated, all the materials such as graphite powder (99.95%), potassium permanganate ( $\text{KMnO}_4$ ), sulphuric acid ( $\text{H}_2\text{SO}_4$ ), hydrogen peroxide ( $\text{H}_2\text{O}_2$ ), hydrochloric acid (HCl), cetyl trimethyl ammonium bromide (CTAB), sodium nitrate ( $\text{NaNO}_3$ ), hydrazine, Iron trichloride ( $\text{FeCl}_3$ ) and dichloromethane ( $\text{CH}_2\text{Cl}_2$ ) were

procured from reputed vendors and were of AR grade. All other reagents used in this work were of analytical grade and were used without further purification.

### 2.2 Instrumentation

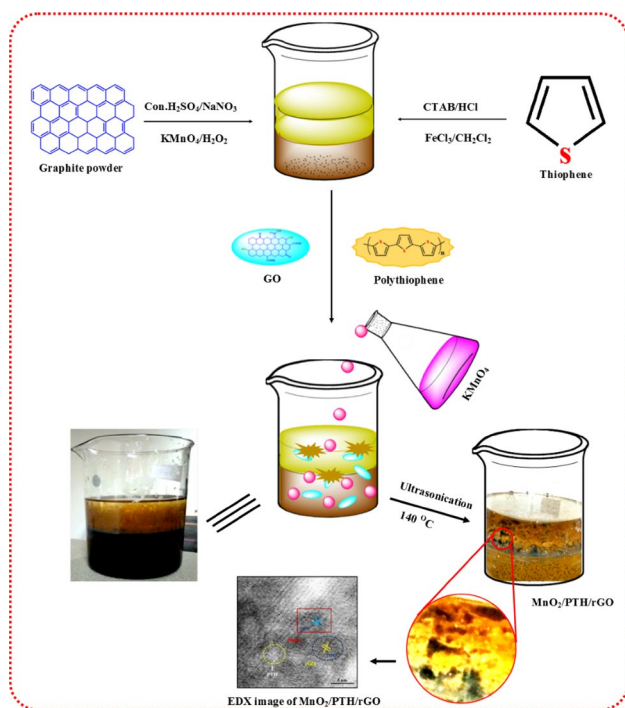
FT-IR spectra was recorded using a Perkin-Elmer IR spectrometer. XRD (Panalytical-Netherlands) X-ray diffraction was used for crystallographic and phase structure characterization of the nanocomposites. Raman spectra were recorded in a micro Raman imaging spectrograph (SEKI, Japan) with a He-Ne laser beam (STR 500 nm). The surface morphology of the nanocomposites characterized using a ZSISS (EVO18-German) scanning electron microscopy (SEM) and INCAX-sigh (JCOL 2100, Japan) higher resolution transmission electron microscope (HR-TEM). The electrochemical studies were performed through a CHI 643 B electrochemical workstation (CHI, USA). The cell consisted with three electrode system which of an Ag/AgCl wire (saturated KCl) as the reference electrode, Pt wire as an auxiliary/counter electrode and either a modified or unmodified glassy carbon electrode (GCE) as the working electrode.

### 2.3 Synthesis of $\text{MnO}_2$ nanopowder

$\text{MnO}_2$  nanoparticles were prepared using the following procedure: 100 ml of 0.005 mM CTAB containing 0.5 M HCl was mixed with 2.5 mM  $\text{KMnO}_4$  solution and refluxed on a magnetic stirrer for 2 h at ice cold condition. After completion of the stirring, the mixed solution was sonicated for 30 min. The resultant dark brown precipitate was filtered and washed with ethanol and deionized water. The filtered fine  $\text{MnO}_2$  precipitate was calcinated at 500 °C for 6 h.

### 2.4 Synthesis of $\text{MnO}_2$ /PTH/rGO nanocomposite

The general procedure for the preparation of  $\text{MnO}_2$ /PTH/rGO nanocomposite by in situ chemical oxidative polymerization method is given in Scheme 1. Firstly, 3 g of graphite powder was dispersed into 300 ml of conc.  $\text{H}_2\text{SO}_4$  under stirring on an ice bath. Then, 1.5 g of  $\text{NaNO}_3$  and 2.5 g of  $\text{KMnO}_4$  was added slowly and stirred in ice cold condition (0–5 °C) for 30 min. After that, the mixture was heated (oil bath) at 98 °C followed by addition of 200 ml of double distilled water. When the mixture reached a temperature of 50 °C, the reaction was terminated by addition of 10 ml of 30% ice cold  $\text{H}_2\text{O}_2$  in a sequential manner to reduce the residual oxidant and stirred for 24 h on an ice bath. This solution was termed as “A”. Then, 0.5 ml of thiophene (monomer) and 0.005 mM of surfactant CTAB (containing 0.5 M HCl) solutions were taken in a separate flask and stirred for 30 min at ice cold condition. Then, 2.0 g of  $\text{FeCl}_3$  and 50 ml  $\text{CH}_2\text{Cl}_2$  suspension mixture was added to the above mixture



**Scheme 1** Schematic representation of preparation of  $\text{MnO}_2/\text{PTH}/\text{rGO}$  nanocomposite

and vigorously stirred for 30 min. This solution was termed as “B”.

Then, the mixture of A was added into B to form the organic and inorganic interface. Similarly, 0.5 mg of  $\text{KMnO}_4$  (fine powder) was added again to initiate the polymerization, during which,  $\text{MnO}_4^-$  was converted to  $\text{MnO}_2$  concurrently. The suspension mixture of aquatic and organic interface was subjected to ultrasonication (3 h at  $140^\circ\text{C}$ ) for the formation of GO, which was subsequently reduced to rGO and uniformly distributed over the PTH film. Finally, the dark brown precipitate of  $\text{MnO}_2/\text{PTH}/\text{rGO}$  nanocomposite was collected by filtration using membrane filter and washed with acetone and double distilled water. The precipitate was dried under vacuum at  $60^\circ\text{C}$  for 24 h. Similarly, rGO and PTH were synthesized using the same procedure, without the addition of polymer and graphene material. Herein, we report the in-house in situ synthesis of the nanocomposite material for the first time.

## 2.5 Preparation of modified electrode ( $\text{MnO}_2/\text{PTH}/\text{rGO}$ )

The glassy carbon electrode was polished carefully with  $0.05\ \mu\text{M}$  alumina slurries and sonicated for 10 min using ethanol and double distilled water. After sonication, it was dried under nitrogen atmosphere for 10 min. A suspension mixture of electrode materials was prepared by adding

10 mg of  $\text{MnO}_2/\text{PTH}/\text{rGO}$  nanohybrid composite, 0.1 ml 5% nafion solution, 200  $\mu\text{l}$  of 99.9% ethanol and 100  $\mu\text{l}$  of double distilled water. The homogeneous mixture was ultrasonicated for 15 min, following which, 0.7–10  $\mu\text{l}$  of suspension mixture of  $\text{MnO}_2/\text{PTH}/\text{rGO}$  nanocomposite was drop casted on the GC electrode and dried for 30 min at room temperature.

## 2.6 Determination of methyl parathion (MP)

Using cyclic voltammetry (CVs), differential pulse voltammetry (DPV) and amperometry methods, electrochemical reduction of MP was performed by dissolving the pesticide in 0.1 M phosphate buffer solution (PBS) pH 7.0, at a potential range of  $-1.0\ \text{V}$  to  $+0.2\ \text{V}$ . The PB electrolyte solution was purged with nitrogen for 10 min. Care was taken to maintain an inert nitrogen atmosphere during the measurements.

## 2.7 Preparation of real samples

Human urine and blood samples were collected from a local hospital. The urine sample was centrifuged for 20 min at 10,000 rpm. The clear supernatant was collected as stock solution and subsequently used for real sample analysis. Prior to analysis, the serum was stored  $-4^\circ\text{C}$ . 1 ml of both urine and serum sample was diluted with 20 ml of PB solution (pH 7) and known concentration of MP was spiked into the solution. Finally, the prepared real samples were analyzed by using the  $\text{MnO}_2/\text{PTH}/\text{rGO}$  nanocomposite sensor we had fabricated.

## 3 Results and discussion

### 3.1 Characterization of $\text{MnO}_2$ , rGO, PTH and $\text{MnO}_2/\text{PTH}/\text{rGO}$ nanocomposite

The structural and functional surface of the synthesized nanomaterials was characterized using FTIR and XRD. Figure 1a depicts the FTIR spectrum of pure  $\text{MnO}_2$  which displayed the absorption peaks at 702, 521 and  $573\ \text{cm}^{-1}$  corresponding to (O–Mn–O) and (Mn–O) stretching vibrations, respectively [34, 35]. The FTIR spectrum of PTH film was shown in [Fig. 1b]. It displayed the characteristic absorption peaks at 1136, 1640 and  $1414\ \text{cm}^{-1}$  which indicated the C–H in-plane bending, asymmetric and symmetric stretching vibration bands of C=C, respectively. The absorption peaks of C–H (out of plane stretching vibration), C–S (bending vibration) appeared at 786,  $656\ \text{cm}^{-1}$ , which indicates the 2, 5-substituted thiophene ring and thiophene monomer were presented in polymer chain (polythiophene) [36–38]. It was also interesting to observe [Fig. 1c] the characteristic peaks

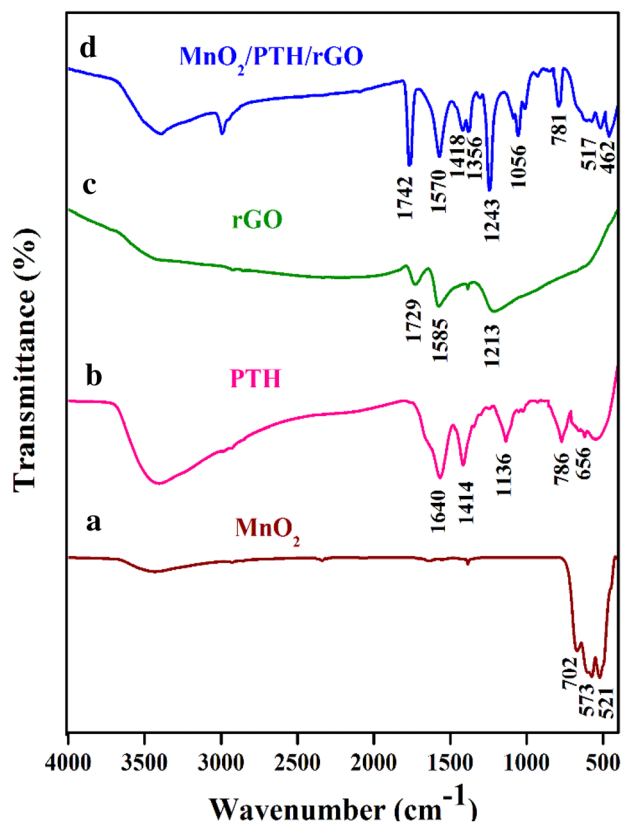


**Fig. 1** FTIR spectra of MnO<sub>2</sub> (a), PTH (b), rGO (c) and MnO<sub>2</sub>/PTH/rGO (d)

of rGO at 1729, 1585 and 1213 cm<sup>-1</sup> corresponding to C=O in COOH, C=C and C–O which revealed that carboxylic and aromatic ring vibration of rGO [39, 40]. With reference to the vibrational modes observed for the individual compounds with the composite, the strong absorption peak at 786 cm<sup>-1</sup> was ascribed to C–H out of plane stretching vibration of PTH (weakened), which had shifted to a lower wavenumber (781 cm<sup>-1</sup>), which illustrated that PTH was incorporated with MnO<sub>2</sub> successfully. Furthermore, when peaks for individual materials were compared with that for the nanocomposite (curve a–c), a novel peak appeared at 462 cm<sup>-1</sup> [Fig. 1 curve (d)], which corresponds to C–S–C ring deformation. The FTIR results showed characteristic peaks of both the components and thereby revealed the successful incorporation of MnO<sub>2</sub> and rGO on the surface of the PTH matrix.

The crystalline nature, purity and phase of MnO<sub>2</sub>, PTH, rGO and the MnO<sub>2</sub>/PTH/rGO nanocomposite was determined by X-ray diffraction (XRD) technique. As shown in Fig. 2, the XRD pattern of MnO<sub>2</sub> (curve a) displayed the characteristic absorption peaks at 32.46°, 37.74°, 54.72° and 65.26°, which corresponded well to (101), (121), (530) and (002) diffraction pattern of tetragonal MnO<sub>2</sub> (JCPDS no. 72-1982). Yuge et al. [41] reported that the 2θ peak at 37.74° corresponds to (101)

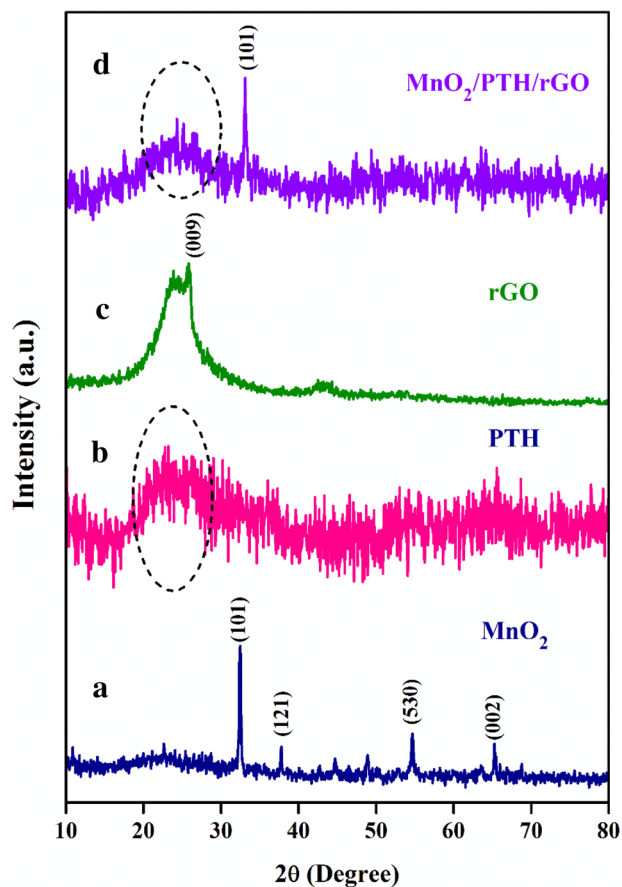


**Fig. 2** X-ray diffraction of MnO<sub>2</sub> (a), PTH (b), rGO (c) and MnO<sub>2</sub>/PTH/rGO (d)

plane of high crystalline MnO<sub>2</sub> nanoparticle. The XRD pattern of PTH (curve b) shows a broad, amorphous diffraction peak at approximately 2θ = 15°–25°. The strong diffraction peak associated with the chain-to-chain stacking (π–π) centered at 2θ = 23° is due to the amorphously packed polythiophene chain [36, 42]. The XRD pattern of rGO (curve c) revealed that the broad characteristic peaks at 25.94° could be well assigned to (009) plane of rGO [43], which confirms the rhombohedral crystalline structure based on the standard data file (JCPDS no. 79-1472). The XRD pattern of MnO<sub>2</sub>/PTH/rGO nanocomposite is shown in Fig. 2d; it reveals that the structure of the metal oxides was not affected by the PTH treatment. On the other hand, the MnO<sub>2</sub> and rGO diffraction peaks were weakened significantly, which could perhaps be a part of distortion in the crystal structure of MnO<sub>2</sub> since its crystal structure was altered into amorphous phase during the polymerization reaction. The average diameter of the crystalline size (*D*) of MnO<sub>2</sub>, rGO and MnO<sub>2</sub>/PTH/rGO nanocomposite (as synthesized) was calculated using the Debye-Scherrer's Eq. (1)

$$D = \frac{k\lambda}{\beta \cos\theta} \quad (1)$$

where,  $k$  is a constant (0.9),  $\lambda$  is X-ray wavelength (Cu- $k\alpha$  radiation = 1.5418 Å),  $\beta$  is the full-width-half-maximum (FWHM) of angle of diffraction (in radians), and  $\theta$  is the Bragg's diffraction angle at maximum intensity. The average particle size of MnO<sub>2</sub>, rGO and MnO<sub>2</sub>/PTH/rGO amorphous nanocomposite film was found to be 30.8, 55.8 and 50–70 nm, respectively. These results were in good agreement with the HRTEM image of nanocomposites.

### 3.2 Raman spectroscopy analysis

Raman spectroscopy measurements were used to confirm the formation of structure-property of the as-synthesized nanocomposite. Figure S1 showed the Raman spectra of MnO<sub>2</sub>, PTH, rGO and MnO<sub>2</sub>/PTH/rGO composite. MnO<sub>2</sub> presented (curve a) a characteristic peak at 706 cm<sup>-1</sup> corresponding to Mn–O lattice vibrations [44]. Figure S1 (curve b) displayed the Raman spectra of the PTH film. In general, the Raman spectra of the PTH film presented in two main lines coupled to the electronic transition. The main dominant lines of the PTH film were centered at 1450 and 639 cm<sup>-1</sup>, which was assigned to the symmetric C=C ring stretching vibration of the conjugated PTH segment and C–S–C ring deformation [45, 46]. Figure S1 (curve c) shows the Raman spectrum of rGO. It showed two characteristic peaks at 1396 and 1642 cm<sup>-1</sup>, corresponding to the D and G bands, respectively [47–49]. The Raman active D and G bands were associated with the first-order Raman scattering of the E<sub>2g</sub> vibrational mode and sp<sup>2</sup> bonded hybridized carbon atoms, respectively. In addition, the Raman bands of MnO<sub>2</sub>, PTH and rGO have been found in the MnO<sub>2</sub>/PTH/rGO composite. Figure S1 (curve d) exhibited the characteristic bands corresponding to MnO<sub>2</sub> (480–780 cm<sup>-1</sup>) and PTH (630 cm<sup>-1</sup>). In contrast to the Raman spectrum of rGO, the intensity ratio of D/G band was slightly higher, which suggested the presence strong interaction of rGO in the MnO<sub>2</sub>/PTH/rGO nanocomposite.

### 3.3 Surface morphological studies of MnO<sub>2</sub>, PTH, rGO and MnO<sub>2</sub>/PTH/rGO nanocomposite

Figure 3 showed the SEM images of as-synthesized MnO<sub>2</sub>, PTH, rGO and the MnO<sub>2</sub>/PTH/rGO nanocomposite. Figure 3a reveals that MnO<sub>2</sub> exhibits uniformly distributed spherical morphology structure. The SEM image of PTH appeared to be akin to amorphous and crushed paper-like structure (Fig. 4b). The reason underlying this appearance may be the rate of different oxidants (CTAB and APS) involved during the polymerization process. Figure 3c displays different sheet and rod-like structures of rGO. Figure 3d shows the SEM image of the composite material and confirms that the MnO<sub>2</sub> and rGO nanomaterials were uniformly distributed on the PTH film surface through the electrostatic attraction of

PTH and rGO via  $\pi$ – $\pi$  conjugated interactions [36]. Furthermore, the morphology of MnO<sub>2</sub>, PTH, rGO and the MnO<sub>2</sub>/PTH/rGO composite were examined by HRTEM. From Fig. 4a, it is apparent that pure MnO<sub>2</sub> displayed an oval-shaped morphology with an average particle size ranging from 30 to 60 nm. Figure 4b depicts the single layer film-like structure of PTH. The HRTEM image of rGO displayed an irregular rod and sheet-like morphological structure (Fig. 4c). Additionally, the HRTEM image of MnO<sub>2</sub>/PTH/rGO (Fig. 4d) composite revealed that the MnO<sub>2</sub> and rGO nanomaterials were uniformly coated with a layer of amorphous PTH film. The above results indicate the presence of MnO<sub>2</sub> and rGO nanomaterials on the surface of PTH, which may be due to  $\pi$ – $\pi$  interactions.

Figure 4e showed clear lattice fringes with interplanar spacing of MnO<sub>2</sub> (0.324 nm) and rGO (0.259 nm). The adjacent planes in the image correspond to the distance of the (101) and (009) planes in tetragonal and rod-like structure of MnO<sub>2</sub> and rGO, respectively. The lattice fringes of PTH were not observed because PTH was amorphous in nature. In addition, energy dispersive X-ray spectrum (EDS) was obtained from the area of MnO<sub>2</sub>/PTH/rGO composite (Fig. 4f), which indicated the major signals of C, Mn, O and S, as expected due to the presence of rGO, MnO<sub>2</sub> and PTH. The C map clearly identified the rGO structure and Mn and O map indicated the presence of MnO<sub>2</sub> as well as the surface map identified the polymer-rich areas of PTH. The EDS results for MnO<sub>2</sub>/PTH/rGO composite suggested the effective doping of MnO<sub>2</sub> and rGO nanomaterials on the surface of PTH film.

### 3.4 Evaluation of the surface area of the modified electrode

The surface areas of the modified electrode was explored using cyclic voltammetry (CV). The cyclic voltammograms (CVs) recorded for 1 mM [Ru(NH<sub>3</sub>)<sub>6</sub>]Cl<sub>3</sub> at MnO<sub>2</sub>/PTH/rGO composite modified electrode and bare GC electrode are shown in Figure S2. Randles–Sevcik equation [50] (shown below) was used for calculating the modified surface area.

$$i_p = 2.69 \times 10^5 n^{3/2} A D^{1/2} C \nu^{1/2} \quad (2)$$

where,  $n$  is number of electrons involved ( $n=1$  for [Ru(NH<sub>3</sub>)<sub>6</sub>]<sup>3+/2+</sup> redox probe),  $A$  is the electroactive surface area (cm<sup>2</sup>),  $D$  is the diffusion coefficient of the [Ru(NH<sub>3</sub>)<sub>6</sub>]<sup>3+/2+</sup> ( $9.1 \times 10^{-6}$  cm<sup>2</sup> s<sup>-1</sup>),  $C$  is the concentration of [Ru(NH<sub>3</sub>)<sub>6</sub>]<sup>3+/2+</sup> (1 mM) and  $\nu$  is the scan rate (V s<sup>-1</sup>). The electroactive surface area of the bare GC and nanocomposite modified electrode was found to be 0.05 cm<sup>2</sup> and 0.0782 cm<sup>2</sup>, respectively. It was observed that the effective surface area of the modified MnO<sub>2</sub>/PTH/rGO GC electrode was significantly increased, which was about 1.5 times

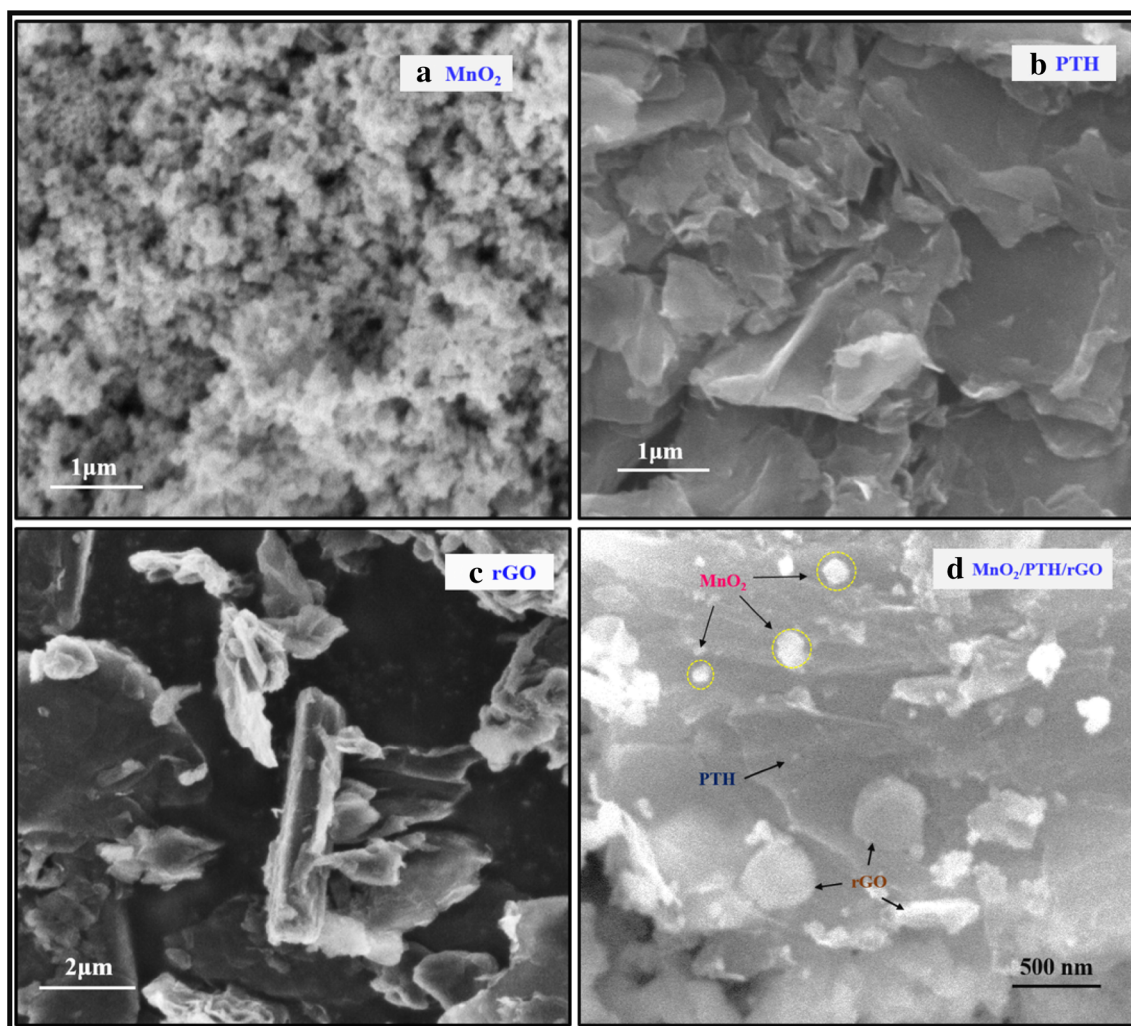


**Fig. 3** SEM image: MnO<sub>2</sub> (a), PTH (b), rGO (c) and MnO<sub>2</sub>/PTH/rGO (d)

higher than the bare GC electrode due to the porous structure of nanocomposite.

### 3.5 Electrochemical impedance spectroscopy

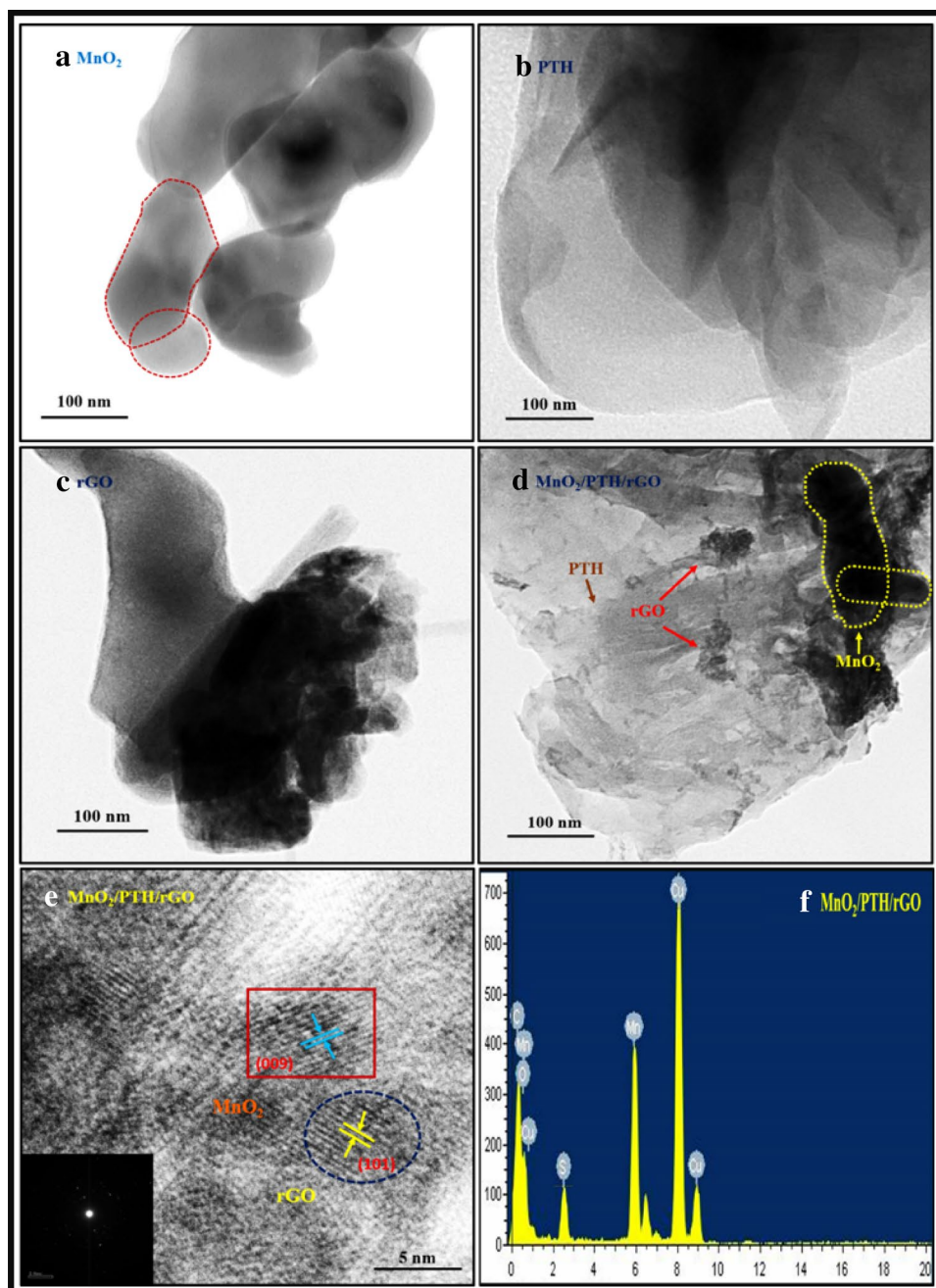
The electrochemical impedance spectroscopy (EIS) was used to investigate the electrical properties of the nanocomposite modified electrode. Figure 5 displayed the EIS of the bare GC and MnO<sub>2</sub>/PTH/rGO modified GC electrodes in 0.1 M KCl solution containing 5 mM K<sub>3</sub>[Fe(CN)<sub>6</sub>]. Randles equivalent circuit model was used to fit the experimental data (inset to Fig. 5) showing the semicircles of  $R_s$ ,  $R_{ct}$ ,  $C_{dl}$  and  $Z_w$ , representing electrolyte resistance, charge transfer resistance, double layer capacitance and Warburg impedance, respectively. The EIS spectrum of the bare GC showed the large semicircle with the charge transfer resistance ( $R_{ct}$ ) of 202  $\Omega$ . On the other hand, the MnO<sub>2</sub>/PTH/rGO modified electrode showed an  $R_{ct}$  of 93  $\Omega$ . The EIS results confirmed

that the conductance of the MnO<sub>2</sub>/PTH/rGO modified electrode was higher than that of the bare GC electrode.

### 3.6 Electrochemical reduction of MP at different modified electrodes

Electrocatalytic activity of the MnO<sub>2</sub>/PTH/rGO nanocomposite modified electrode towards the reduction of 100  $\mu$ M MP was investigated in 0.1 M PBS (pH 7.0) at a scan rate of 50  $\text{mV s}^{-1}$  in the potential range of +0.2 to  $-1.0$  V. Figure 6a compares the electrochemical performance of bare GC and different modified electrodes towards 100  $\mu$ M MP. Among the different electrodes, the MnO<sub>2</sub>/PTH/rGO modified electrode showed higher reduction current in the presence of MP. From the CVs, the reduction current of MP at the MnO<sub>2</sub>/PTH/rGO composite was found to be  $-14.63$   $\mu$ A, whereas, the reduction current of  $-4.70$ ,  $-8.44$   $\mu$ A,  $-6.40$  and  $-9.97$   $\mu$ A at bare GC, MnO<sub>2</sub>, rGO and MnO<sub>2</sub>/PTH

**Fig. 4** HRTEM image: MnO<sub>2</sub> (a), PTH (b), rGO (c) and MnO<sub>2</sub>/PTH/rGO (d) Lattice fringes (e) and EDX of MnO<sub>2</sub>/PTH/rGO (f)



modified electrodes, respectively. The higher electrocatalytic activity obtained at the nanocomposite modified electrode was attributed to the higher electrochemically active area and synergistic effect of MnO<sub>2</sub> and rGO with PTH. Moreover, the presence of  $\pi$  electrons at the MnO<sub>2</sub>/PTH/rGO electrode facilitated MP interaction via  $\pi$ - $\pi$  stacking. Besides, the large conductivity of the MnO<sub>2</sub>/PTH/rGO composite also contributed to the augmentation of MP reduction current.

Figure 6b shows two consecutive voltammograms of the MnO<sub>2</sub>/PTH/rGO modified GC electrode. In the first cycle (peak a; solid line), a cathodic peak was observed at

-0.68 V due to the irreversible reduction of -NO<sub>2</sub> group of MP to -NHOH group via a four electron transfer process (Scheme 2). Through the reverse scan, reversible redox peaks (peak b and c) were observed, which were identified as redox reactions leading to conversion of -NHOH group to -NO group; the oxidation and reduction peaks of b and c observed at 0.05 and 0.15 V (dotted line) are apparent. The pair of reversible redox peaks may be due to a two-electron transfer redox process. The obtained electrochemical behavior of MP was consistent with previously published papers [7, 27].

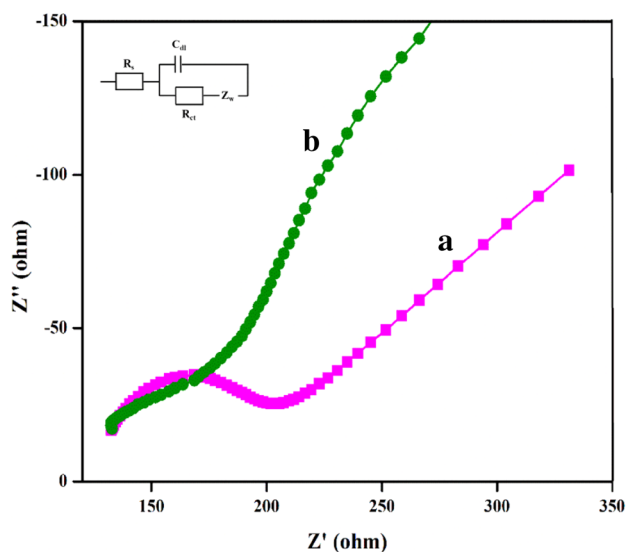


**Fig. 5** EIS of bare GCE (a) and the  $\text{MnO}_2/\text{PTH}/\text{rGO}$  modified GCE (b) in 0.1 M KCl containing 5 mM  $[\text{Fe}(\text{CN})_6]^{3-/4-}$

### 3.7 Effect of pH

The effect of pH on the response of MP reduction was studied using the  $\text{MnO}_2/\text{PTH}/\text{rGO}$  modified electrode over the range of pH (6, 6.5, 7, 7.5 and 8) 6 to 8 in 0.1 M PBS. As shown in Figure S3, the peak current was increased from pH 6 to 7 and then decreased on further increasing from 7 to 8. The best electrochemical response of the

irreversible cathodic peak current was obtained at pH 7. Hence, we have chosen pH 7 for further electrochemical experiments. The plot between pH and current is given in Fig. 7a. The plot of various pH versus peak potential revealed good linearity with the correlation coefficient of  $R^2 = 0.9959$  (Fig. 7b).

### 3.8 Effect of scan rate and concentration

The effect of potential scan rate on the reduction of MP was studied by recording different scan rates from 10 to 100  $\text{mVs}^{-1}$ . We can infer from Fig. 8a that the reduction peak had shifted to a more negative value (from  $-0.65$  to  $-0.70$  V) for MP, particularly with increasing scan rates along with a concurrent increase in current. Similarly, the oxidation peak potential of MP had also shifted slightly towards the positive side (from 0.014 to 0.058 V) along with an increase in the peak current, exhibiting a good liner relationship between the scan rate and peak current (Fig. 8b) with a correlation coefficient of  $R^2 = 0.9974$ . Hence, this phenomenon indicated that the oxidation and reduction of MP was kinetically controlled at surface of the  $\text{MnO}_2/\text{PTH}/\text{rGO}$  modified electrode. Figure 8c exhibited the reduction of MP at different concentrations ranging from 50  $\mu\text{M}$  to 500  $\mu\text{M}$  by the  $\text{MnO}_2/\text{PTH}/\text{rGO}$  nanocomposite-doped glassy carbon electrode. The oxidation and reduction peak current was increased with increasing the concentration of MP linearly, with the correlation coefficient of  $R^2 = 0.9911$ , which is shown in Fig. 8d.

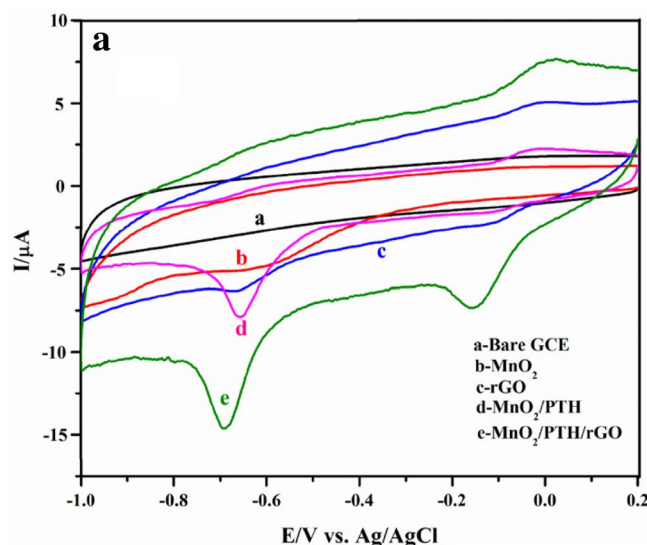
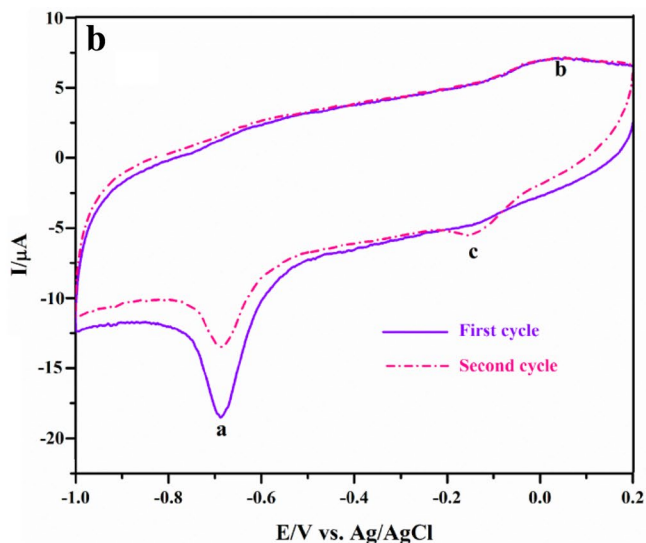
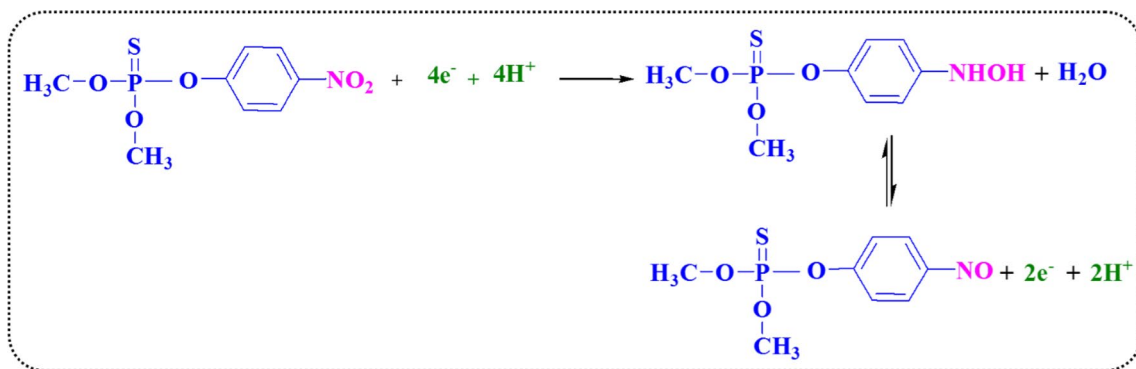


**Fig. 6** **A** Cyclic voltammograms obtained for different modified electrodes (a) bare GCE, (b)  $\text{MnO}_2$ , (c) rGO, (d)  $\text{MnO}_2/\text{PTH}$  and (e)  $\text{MnO}_2/\text{PTH}/\text{rGO}$  modified GCE. **B** Two continuous cyclic voltammo-



grams of  $\text{MnO}_2/\text{PTH}/\text{rGO}$  modified GCE towards electrocatalysis of 100  $\mu\text{M}$  MP in 0.1 M PBS (pH 7), scan rate 50  $\text{mV s}^{-1}$





**Scheme 2** Mechanism of the electrochemical reaction of MP at MnO<sub>2</sub>/PTH/rGO nanocomposite modified electrode

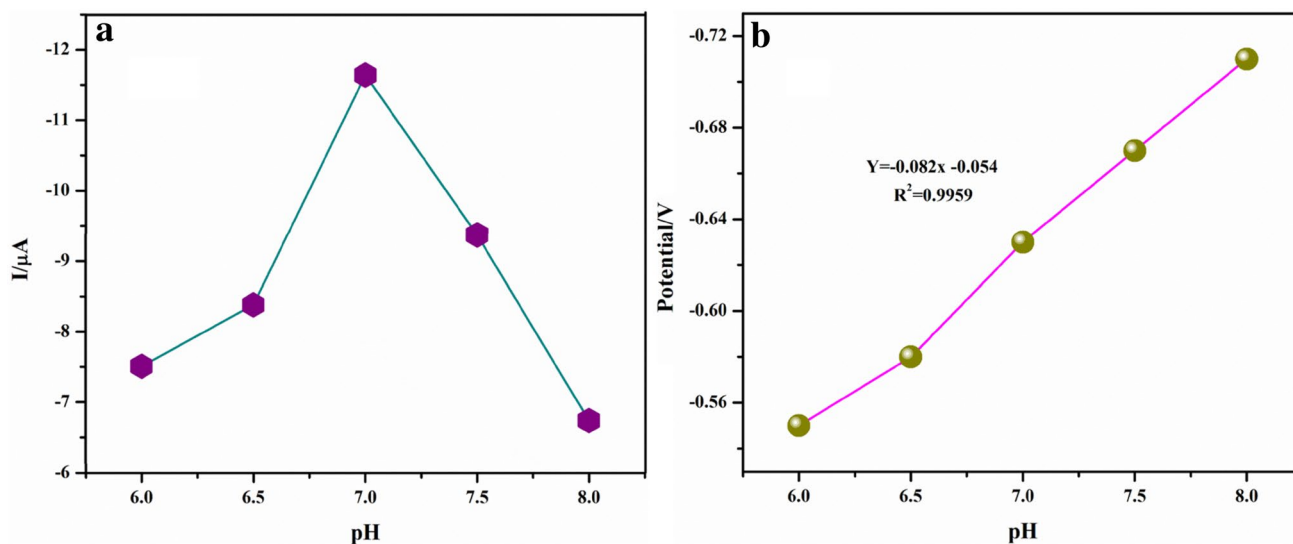


**Fig. 7** **a** The voltammograms were performed using MnO<sub>2</sub>/PTH/rGO/GEC in phosphate buffer solution (pH 7.0) containing 100 μM MP to assess the effect of pH. **b** Dependence of cathodic peak potential with pH

### 3.9 Calculation of the number of electrons from Laviron equation

The irreversible nature of the reduction of MP at the modified MnO<sub>2</sub>/PTH/rGO GC electrode could be found by the cathodic peak potential with respect to the scan rate in the cyclic voltammogram. Figure 9 exhibited that the irreversible reduction peak potential increased linearly with log  $\nu$ . According to the Laviron equation [32].

$$y = 2.303 RT / \alpha n_a F \times \log \left( RTk_f^0 / \alpha n_a F \nu \right) \quad (3)$$

where,  $n_a$  is the number of electrons transferred,  $\alpha$  is the transfer coefficient,  $k_f^0$  is the standard heterogeneous rate constant,  $R$  is the universal gas constant (in J K<sup>-1</sup> mol<sup>-1</sup>),  $F$  is the Faraday constant,  $T$  represents Temperature (in K),  $E_p$  is the cathodic peak potential and  $\nu$  is the sweep rate

(in V s<sup>-1</sup>). Through the reduction process, we deduced the number of electrons transferred from the slope of the plot between  $E_{pc}$  versus log  $\nu$ . The total number of electrons transferred for the reduction of MP ( $n_a$ ) was found to be 3.58. Thus it was evidenced that the irreversible reduction of MP involved four electrons transfer on the modified MnO<sub>2</sub>/PANI/rGO GCE. Thereby, we confirm that the reduction reaction involves conversion of the nitro group in MP to phenylhydroxylamine group.

### 3.10 Sensitive determination of MP by differential pulse voltammetry

Differential pulse voltammetry can be used to quantitatively detect MP residues and it was more sensitive than that of other voltammetry techniques. Figure 10a displayed the DPV responses of MP at various concentrations

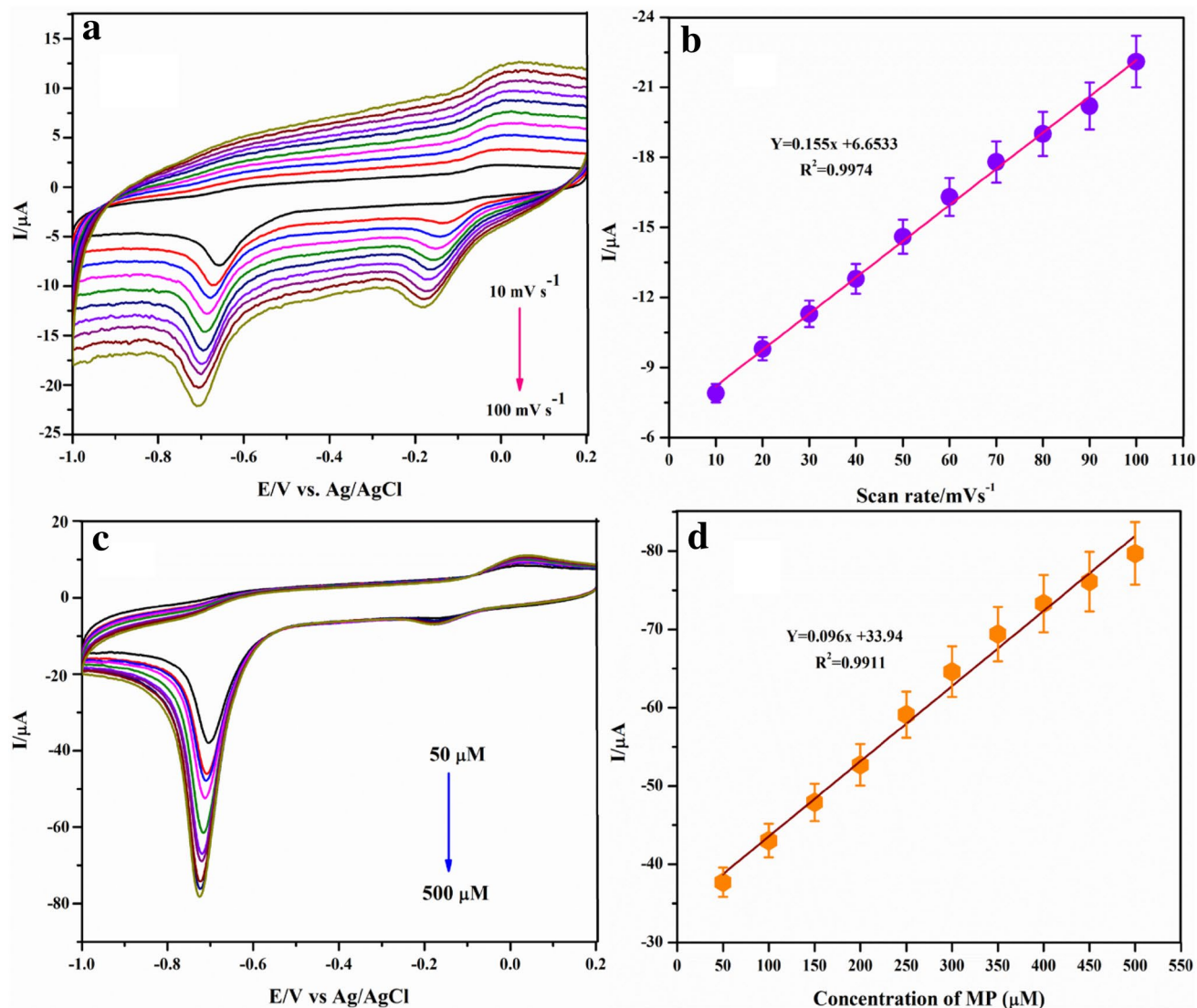


**Fig. 8** **a** Cyclic voltammograms obtained using MnO<sub>2</sub>/PTH/rGO composite modified electrode at various scan rates (10–100  $\text{mV s}^{-1}$ ). **b** Calibration plot of scan rate ( $\text{mV s}^{-1}$ ) vs peak current ( $\mu\text{A}$ ). **c** Cyclic voltammograms of MnO<sub>2</sub>/PTH/rGO in PBS (pH 7.0) containing a range of MP concentration (50–500  $\mu\text{M}$ ) at a scan rate 50  $\text{mV s}^{-1}$ . **d** Calibration plot of current ( $\mu\text{A}$ ) versus concentration [MP]/ $\mu\text{M}$

towards the MnO<sub>2</sub>/PTH/rGO composite in PBS (pH 7). The linear range is from 0.5 to 65  $\mu\text{M}$ . It was observed that increase in reduction peak current was proportional to the concentration of MP in a linear fashion. Figure 10b exhibited the linear calibration plot between the peak current ( $I_p$ ) and different concentration of MP with a correlation coefficient of  $R^2 = 0.9941$ . The modified electrode (MnO<sub>2</sub>/PTH/rGO) showed better performance for MP reduction due to the higher electron transfer rate and remarkable catalytic properties of the MnO<sub>2</sub>/PTH/rGO composite. Therefore, the MnO<sub>2</sub>/PTH/rGO nanocomposite modified electrode can be used as an excellent electrode material for the detection of MP.

taining a range of MP concentration (50–500  $\mu\text{M}$ ) at a scan rate 50  $\text{mV s}^{-1}$ . **d** Calibration plot of current ( $\mu\text{A}$ ) versus concentration [MP]/ $\mu\text{M}$

### 3.11 Amperometry analysis

Amperometry was performed to assess the responses of MnO<sub>2</sub>/PTH/rGO towards sequential addition of MP in 0.1 M PBS at pH 7.0 by applying a constant potential of +0.50 V [Fig. S4 (A)]. For each addition (10 nM to 1  $\mu\text{M}$ ), the appearance of response current and 95% of steady state current was reached within 3 s. The linear increase of MP and its response (of increasing peak current) indicated the exceptional electrocatalytic response of MP reduction using the MnO<sub>2</sub>/PTH/rGO nanocomposite-modified electrode. The Inset in Fig. S4(B) shows the concentration-dependent linear calibration plot with a correlation coefficient of  $R^2 = 0.9917$ .

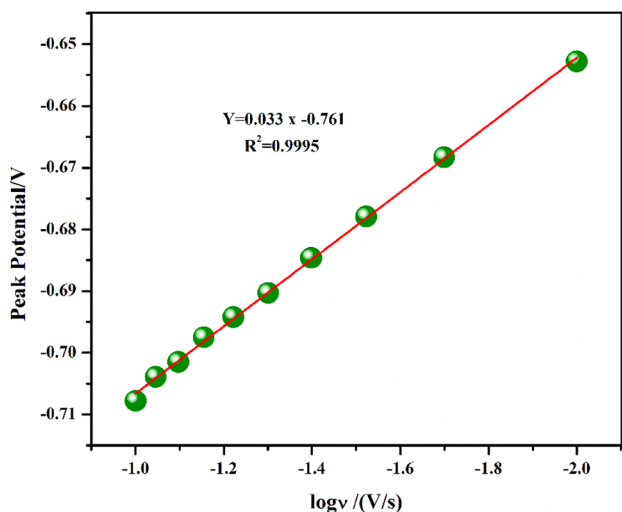


Fig. 9 Plot of irreversible peak potential of MP versus  $\log \nu$

The limit of detection (LOD) was found to be 5.72 nM and the sensitivity was  $0.0498 \mu\text{A } \mu\text{M}^{-1} \text{cm}^{-2}$ . The significant parameters of the sensor, such as linear range and LOD, were compared to the various previously reported modified electrodes used as pesticide sensors (Table 1).

### 3.12 Real sample analysis

The present nanocomposite modified electrode was used to determine MP in real samples (human urine and serum). The standard addition technique was used to determine trace concentrations of MP in real samples. Figure 11a, b showed the DPVs of human blood serum and urine samples in 0.1 M PBS (pH 7) with the linear addition of different micromolar concentrations (a–f). Figure 11a, b exhibited the presence of MP in both serum and urine samples, and exhibited sharp reduction peaks at  $-0.65 \text{ V}$ . From the results, the sensor parameters of LOD and sensitivity of MP in blood serum and urine sample have been calculated. For blood serum sample, the LOD and sensitivity were 1.3 nM and  $0.1124 \mu\text{A } \mu\text{M}^{-1} \text{cm}^{-2}$ , respectively. For human

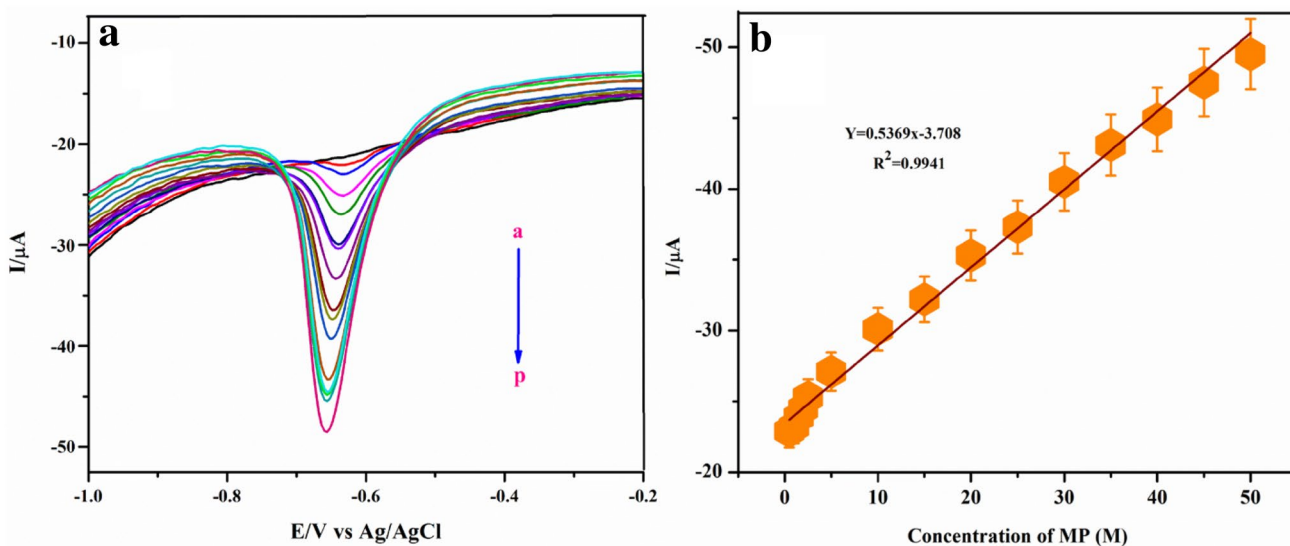
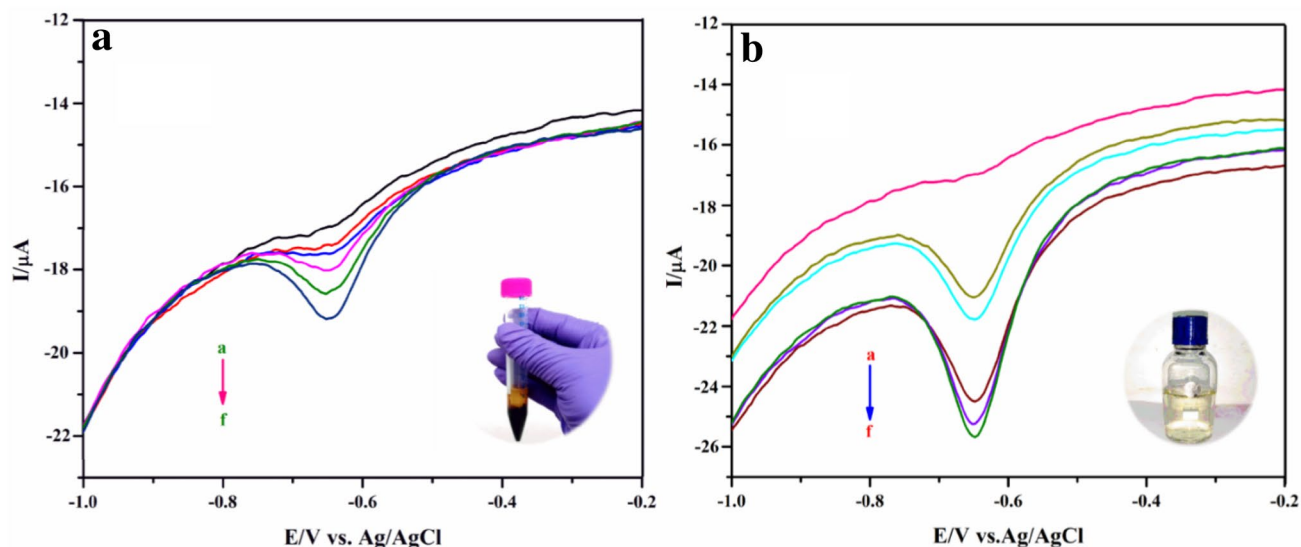


Fig. 10 a DPV responses obtained using  $\text{MnO}_2/\text{PTH}/\text{rGO}/\text{GCE}$  in 0.1 M PBS (pH 7.0) for MP at a range of  $0.5 \mu\text{M}$  to  $65 \mu\text{M}$  (a–p). b Calibration plot of peak current ( $\mu\text{A}$ ) versus  $[\text{MP}]/\mu\text{M}$

**Table 1** Comparison of analytical performance of  $\text{MnO}_2/\text{PTH}/\text{rGO}$  nanocomposite modified GCE with previously reported MP sensors

Electrode	Linear range ( $\mu\text{M}$ )	LOD ( $\mu\text{M}$ )	References
GCE	2–50	0.05	[2]
N-doped carbon dotes (NCDs)	2.38–73.78	0.338	[5]
GQDs/AChE/CHOx (dichlovos and methyl paraoxon)	0.45–45.25	0.78	[19]
PLaE-CS/AuNPs-GNs/GCE	0.56–100	86	[51]
Db-silica/CPE	0.125–2.56	13	[52]
$\text{MnO}_2/\text{PTH}/\text{rGO}/\text{GCE}$	0.5–10	0.00572	Present work



**Fig. 11** A and B DPV obtained using  $\text{MnO}_2/\text{PTH}/\text{rGO}/\text{GCE}$  for real samples (blood serum and urine): (a) exhibits the standard DPV, (b) 0.5  $\mu\text{M}$ , (c) 1.0  $\mu\text{M}$ , (d) 3.0  $\mu\text{M}$ , (e) 5  $\mu\text{M}$  and (f) 10  $\mu\text{M}$  in 0.1 M PBS (pH 7)

**Table 2** Determination of MP in real samples using  $\text{MnO}_2/\text{PTH}/\text{rGO}/\text{GCE}$

Real sample	Amount of MP added/ $\mu\text{M}$	Found/ $\mu\text{M}$	Recovery %	RSD %
Blood serum sample	0.5	0.46	92.2	2.04
	1	0.93	93.9	
	3	2.87	95.9	
	5	4.70	94.1	
	10	9.72	97.2	
Urine sample	0.5	0.47	94.9	3.5
	1	0.96	96.8	
	3	2.81	93.3	
	5	4.10	89.9	
	10	8.42	88.5	

urine samples, the LOD and sensitivity were 4.8 nM and  $0.2809 \mu\text{A} \mu\text{M}^{-1} \text{cm}^{-2}$ , respectively. The corresponding results are given in Table 2. From the experimental results, the nanocomposite ( $\text{MnO}_2/\text{PTH}/\text{rGO}$ ) modified electrode was proved to possess potential practical application and hence, it can be used for detection of MP in clinical samples.

## 4 Conclusions

In the present work, we have successfully synthesized and characterized a new  $\text{MnO}_2/\text{PTH}/\text{rGO}$  nanocomposite via green approach. The nanocomposite  $\text{MnO}_2/\text{PTH}/\text{rGO}$  was utilized to modify the electrode to detect MP at trace levels. The electrochemical response was assessed using CV,

DPV and amperometric techniques. The fabrication of the  $\text{MnO}_2/\text{PTH}/\text{rGO}$  sensor was uncomplicated and the results showed that the sensor possessed commendable attributes such as relative simplicity, effectiveness, high sensitivity and selectivity for detection of MP at low concentrations. Furthermore, the sensor displayed excellent performance over a wide linear range of MP (0.5  $\mu\text{l}$  to 10  $\mu\text{l}$ ) with a detection limit of 5.72 nM. In real samples, the LOD was determined to be 1.3 nM in blood and 4.8 nM in urine. The sensitivity was  $\sim 0.0498$  and  $2.6099$  for blood and urine samples, respectively. The developed sensor exhibited excellent performance for determination of MP in human serum and urine samples. The results indicated that the sensor could be practically applied for the detection of MP in human samples. We are currently working on this aspect. Hence, we surmise that the nanocomposite modified electrode fabricated by us has potential for MP detection in a simple and cost-effective manner.

**Acknowledgements** The authors gratefully acknowledge the Principal and Management of Bishop Heber College, Tiruchirappalli for their support and encouragement. Special thanks to Rajiv Gandhi National Fellowship (University Grants Commission, New Delhi, Ref. No. 43823) for the financial support.

## References

1. A.B. Baranda, A. Lasagabaster, I.M. De Maranon, J. Hazard. Mater. **340**, 140 (2017)
2. D.M. Stankovic, E. Mehmeti, L. Svorc, K. Kalcher, Electroanalysis **27**, 1587 (2015)
3. H.H. Chhipa, Environ. Chem. Lett. **15**, 15 (2017)

4. H. Rasoulnezhad, G. Kavei, K. Ahmadi, M.R. Rahimpour, J. Mater. Sci. Mater. Electron. **28**, 18337 (2017)
5. W. Song, H.J. Zhang, Y.H. Liu, C.L. Ren, H.L. Chen, Chin. Chem. Lett. **28**, 1675 (2017)
6. L. Yang, G.C. Wang, Y.J. Liu, J.J. An, M. Wang, Anal. Bioanal. Chem. **405**, 2545 (2013)
7. M. Govindasamy, S. Sakthnathan, S.M. Chen, T.W. Chiu, A. Sathiyar, J.P. Merlin, Electroanalysis **29**, 1950 (2017)
8. A.A. Ensaifi, F. Rezaloo, B. Rezaei, Electroanalysis **29**, 2839 (2017)
9. K. Huen, A. Bradman, K. Harley, P. Yousefi, D.B. Barr, B. Eskenazi, N. Holland, Environ. Res. **117**, 8 (2012)
10. M. Boisvert, P.B. Fayad, S. Sauve, Anal. Chim. Acta **754**, 75 (2012)
11. S. Chen, Y. Xu, Y. Bi, W. Du, B.F. Liu, Talanta **70**, 63 (2006)
12. J. Wang, H. Suzuki, T. Satake, Sens. Actuators B Chem. **204**, 297 (2014)
13. S. Boulanouar, S. Mezzache, A. Combes, V. Pichon, Talanta **176**, 465 (2018)
14. X. Yang, J. Luo, Y. Duan, S. Li, C. Liu, Food Chem. **241**, 188 (2018)
15. G. Xu, J. Nie, H. Li, Z. Yan, Y. Cheng, Anal. Bioanal. Chem. **409**, 5057 (2017)
16. A. Srivastava, S. Rai, A.K. Sonker, K. Karsauliya, C.P. Pandey, S.P. Singh, Anal. Bioanal. Chem. **409**, 3757 (2017)
17. F. Musshoff, H. Junker, B. Madea, J. Chromatogr. Sci. **40**, 29 (2002)
18. X.H. Lin, S.X. Aik, J. Angkasa, Q. Le, K.S. Chooi, S.F. Li, Sens. Actuators B Chem. **258**, 228 (2018)
19. C. Sahub, T. Tuntulani, T. Nhujak, B. Tomapatanaget, Sens. Actuators B Chem. **258**, 88 (2018)
20. N. Chauhan, C.S. Pundir, Electrochim. Acta **67**, 79 (2012)
21. C.P. Li, S. Fan, C. Yin, N. Zhang, S. Du, H. Zhao, Anal. Methods **6**, 1914 (2014)
22. F. Arduini, S. Cinti, V. Scognamiglio, D. Moscone, Microchim. Acta **183**, 2063 (2016)
23. N. Shams, H.N. Lim, R. Hajian, N.A. Yusof, J. Abdullah, Y. Sulaiman, I. Ibrahim, N.M. Huang, A. Pandikumar, J. Appl. Electrochem. **46**, 655 (2016)
24. M. Xu, J. Zhu, H. Su, J. Dong, S. Ai, R. Li, J. Appl. Electrochem. **42**, 509 (2012)
25. M. Govindasamy, V. Mani, S.M. Chen, T.W. Chen, A.K. Sundramoorthy, Sci. Rep. **7**, 46471 (2017)
26. P.A. Sundari, P. Manisankar, J. Appl. Electrochem. **41**, 29 (2011)
27. J. Fu, X.H. Tan, Y.H. Li, X.J. Song, Chin. Chem. Lett. **27**, 1541 (2016)
28. Y. Wang, J. Jin, C. Yuan, F. Zhang, L. Ma, D. Qin, D. Shan, X. Lu, Analyst **140**, 560 (2015)
29. J. Huang, Y. Kang, T. Yang, Y. Wang, S. Wang, J. Nat. Gas Chem. **20**, 403 (2011)
30. I. Sultana, M. Idrees, M.Y. Rafique, S. Liyas, S.Q. Hussain, A.A. Kahn, A. Razaq, J. Mater. Sci. Mater. Electron. **29**, 20588 (2018)
31. P. Si, P. Chen, D.H. Kim, J. Mater. Chem. B. **1**, 2696 (2013)
32. A.K. Thakur, M. Majumder, R.B. Choudhary, S.N. Pimpalkar, Mater. Sci. Eng. **149**, 012166 (2016)
33. S. Bachhav, D. Patil, J. Nanostructures. **7**, 247 (2017)
34. W. Xiao, J.S. Chen, Q. Lu, X.W. Lou, J. Phys. Chem. C. **114**, 12048 (2010)
35. R. Jamal, L. Zhang, M. Wang, Q. Zhao, T. Abdiryim, Prog. Nat. Sci. Mater. **26**, 32 (2016)
36. J. Zhao, Y. Xie, Z. Le, J. Yu, Y. Gao, R. Zhong, Y. Qin, Y. Huang, Synth. Met. **181**, 110 (2013)
37. Z. Seyedzavar, M. Babazadeh, Synth. React. Inorg. Met.-Org. Chem. **46**, 389 (2016)
38. F. Kong, Y. Wang, J. Zhang, H. Xia, B. Zhu, Y. Wang, S. Wang, S. Wu, Mater. Sci. Eng. B **150**, 6 (2008)
39. L. Wang, Y. Ye, X. Lu, Z. Wen, Z. Li, H. Hou, Y. Song, Sci. Rep. **3**, 3568 (2013)
40. R. Vinoth, S.G. Babu, V. Bharti, V. Gupta, M. Navaneethan, S.V. Bhat, C. Muthamizhchelvan, P.C. Ramamurthy, C. Sharma, D.K. Aswal, Y. Hayakawa, Sci. Rep. **7**, 43133 (2017)
41. Y. Liu, X. Zhang, D. He, F. Ma, Q. Fu, Y. Hu, RSC Adv. **6**, 18654 (2016)
42. Y. Xie, X. Hong, X. Wang, J. Zhao, Y. Gao, Y. Ling, S. Yan, L. Shi, K. Zhang, Synth. Met. **162**, 1643 (2012)
43. G. Han, Y. Liu, E. Kan, J. Tang, L. Zhang, H. Wang, W. Tang, RSC Adv. **4**, 9898 (2014)
44. Z. Awan, K.S. Nahm, J.S. Xavier, Biosens. Bioelectron. **53**, 528 (2014)
45. T. Kitao, M.W. MacLean, B. Le Ouay, Y. Sasaki, M. Tsujimoto, S. Kitagawa, T. Uemura, Polym. Chem. **8**, 5077 (2017)
46. M.R. Karim, C.J. Lee, M.S. Lee, J. Polym. Sci. A Polym. Chem. **44**, 5283 (2006)
47. Q.A. Khan, A. Shaur, T.A. Khan, Y.F. Joya, M.S. Awan, Cogent. Chem. **3**, 1298980 (2017)
48. N. Jarulertwathana, V. Laokawee, W. Susingrat, S.J. Hwang, T. Sarakonsri, J. Mater. Sci. Mater. Electron. **28**, 18994 (2017)
49. P. Bharathidasan, S. Sridhar, P.V. Vardhan, S.R. Sivakkumar, D.W. Kim, S. Devaraj, J. Mater. Sci. Mater. Electron. **29**, 7661 (2018)
50. J.I. Gowda, S.T. Nandibewoor, Asian. J. Pharm. Sci. **9**, 42 (2014)
51. J. Bao, G. Hou, M. Chen, J. Li, D. Huo, M. Yang, X. Luo, Y. Lei, J. Agric. Food Chem. **63**, 10319 (2015)
52. E.M. Caldas, E.W. Menezes, T.M. Pizzolato, S.L.P. Dias, T.M.H. Costa, L.T. Arenas, E.V. Benvenutti, J. Sol-Gel. Sci. Technol. **72**, 282 (2014)

**Publisher's Note** Springer Nature remains neutral with regard to jurisdictional claims in published maps and institutional affiliations.